Nanoscale

ROYAL SOCIETY OF CHEMISTRY

PAPER

View Article Online
View Journal | View Issue

Cite this: *Nanoscale*, 2021, **13**, 14186

Octahedral distortion driven by $CsPbI_3$ nanocrystal reaction temperature – the effects on phase stability and beyond†

Anastasia Matuhina,[a] G. Krishnamurthy Grandhi,[a] Maning Liu,*[a] Jan-Henrik Smått,[b] N. S. M. Viswanath,[c] Harri Ali-Löytty,[d] Kimmo Lahtonen[e] and Paola Vivo*[a]

Cesium lead iodide ($CsPbI_3$) perovskite nanocrystals (NCs) suffer from a known transformation at room temperature from their red-emitting (black) to non-emitting (yellow) phase, induced by the tilting of PbI_6 octahedra. While the reported attempts to stabilize $CsPbI_3$ NCs mainly involve Pb^{2+}-site doping as well as compositional and/or NC surface engineering, the black phase stability in relation only to the variation of the reaction temperature of $CsPbI_3$ NCs is surprisingly overlooked. We report a holistic study of the phase stability of $CsPbI_3$ NCs, encompassing dispersions, films, and even devices by tuning the hot-injection temperature between 120–170 °C. Our findings suggest that the transition from the black to the yellow phase occurs after over a month for NCs synthesized at 150 °C (150@NCs). Structural refinement studies attribute the enhanced stability of 150@NCs to their observed lowest octahedral distortion. The 150@NCs also lead to stable unencapsulated solar cells with unchanged performance upon 26 days of shelf storage in dry air. Our study underlines the importance of scrutinizing synthesis parameters for designing stable perovskite NCs towards long-lasting optoelectronic devices.

Received 23rd June 2021,
Accepted 5th August 2021

DOI: 10.1039/d1nr04071e

rsc.li/nanoscale

1. Introduction

In the plethora of possible halide perovskite compositions, cesium lead iodide perovskite ($CsPbI_3$) remains a key material for single-junction solar cells, since its red-emitting black phase has an optimal bandgap (1.6–1.8 eV)[1] for matching the solar spectrum. Furthermore, being all-inorganic, it has a great potential for developing highly stable perovskite solar cells (PSCs). Yet, the black phase of $CsPbI_3$ is only stable at high temperatures and it otherwise quickly converts to a non-emissive yellow phase with a bandgap (E_g) not suitable for photovoltaic applications.[1] Using high-resolution *in situ* synchrotron X-ray diffraction (XRD) measurements, Marronnier *et al.* demonstrated that $CsPbI_3$ adopts a α-cubic (black) phase only above 645 K, which upon cooling transforms into a β-tetragonal (black) phase (510 K) and then to a metastable γ-orthorhombic (black) phase (325 K). Finally, the γ-orthorhombic (black) phase converts into a δ-orthorhombic (yellow) phase at room temperature.[2–4] The development of perovskite nanocrystals (NCs) has strongly contributed to the stabilization of the black phase of $CsPbI_3$ even at room temperature under specific and well-designed conditions.[5] However, the exposure of $CsPbI_3$ NCs to moisture, light, or heat dramatically (i) reduces their light absorption and photoluminescence (PL) quantum yield (PLQY), (ii) enables phase transitions, and (iii) affects morphological transformations.[6] Recently, substantial improvements in the phase stability of $CsPbI_3$ NCs have been achieved through multiple approaches, such as compositional engineering,[7,8] doping,[9,10] addition of protective ligands (*e.g.* phosphonic acid and ammonium ions),[11,12] as well as variations in the synthesis and purification protocols (*e.g.* weakly polar solvents during purifications).[5] Among the proposed modifications of the well-established hot-injection synthesis (*e.g.* ligand optimization, precursors ratio, reaction temperature), the tuning of the hot-injection temperature is a known approach to mainly control the size of the NCs and, therefore, their E_g and PL.[5,13]

[a]*Hybrid Solar Cells, Faculty of Engineering and Natural Sciences, Tampere University, P.O. Box 541, FI-33014 Tampere, Finland. E-mail: paola.vivo@tuni.fi, maning.liu@tuni.fi*
[b]*Laboratory of Molecular Science and Engineering, Åbo Akademi University, Henriksgatan 2, FI-20500 Turku, Finland*
[c]*School of Materials Science and Engineering, Chonnam National University, 77 Yongbong-ro, Buk-gu, Gwangju, 61186, Republic of Korea*
[d]*Surface Science Group, Faculty of Engineering and Natural Sciences, Tampere University, P.O. Box 692, FI-33014 Tampere, Finland*
[e]*Faculty of Engineering and Natural Sciences, Tampere University, P.O. Box 692, FI-33014 Tampere, Finland*

†Electronic supplementary information (ESI) available: Characterization, XPS study, structural analysis, optical stability study, photophysical study, morphological stability study, and performance of $CsPbI_3$ NCs-based solar cells. See DOI: 10.1039/d1nr04071e

Nevertheless, the stability of the black phase of $CsPbI_3$ NCs in relation to the variation of the reaction temperature is surprisingly underrepresented in the literature. One exception is provided by Dutta *et al.*, who reported the tuning of the hot-injection temperature at higher values than the commonly adopted ones (160–180 °C).[14] In that work, the synthesis of $CsPbI_3$ NCs at a high reaction temperature (260 °C) enabled phase-stable $CsPbI_3$ NCs up to 30 days under ambient conditions *via* strong binding of alkylammonium ligands to the NC surface. However, no study has outlined if long-term phase stability of $CsPbI_3$ NCs can be achieved by tuning the hot-injection temperature below the typically reported values (160–180 °C) and without the need of demanding ligand engineering. Furthermore, the correlation between the temperature of NC synthesis and the stability of the corresponding PSCs, where the NCs are employed as light-harvesters, is still unclear.

In this work, we report a holistic study of the phase stability of $CsPbI_3$ NCs, encompassing dispersions, films, and even devices based on the targeted perovskite nanomaterials. We monitor the changes in the optical (PL), photophysical (time-resolved PL, TRPL), structural (XRD), and morphological (transmission electron microscope, TEM) properties of $CsPbI_3$ NCs synthesized by a well-known hot-injection protocol, in the presence of standard oleic acid/oleylamine ligands, at a reaction temperature between 120–170 °C. The transition from the black (γ-orthorhombic) to the yellow (δ-orthorhombic) phase of $CsPbI_3$ NCs occurs only after 33 days of storage under ambient conditions (RH = 40%, T = 25 °C), when the hot-injection temperature is set to 150 °C. The corresponding unencapsulated PSCs, employing the NCs formed at 150 °C, fully retain their initial performance upon 26 days of shelf storage in dry air.

2. Results and discussion

We synthesized $CsPbI_3$ NCs by following a reported hot-injection synthetic route with minor adaptations,[8] in which the injection temperature was tailored in the range of 120–170 °C (see Experimental section for further details). Briefly, Cs-oleate precursor was swiftly injected into PbI_2 precursor solution at the tuned temperatures of 120 °C, 135 °C, 150 °C, and 170 °C, referred hereafter as 120@NCs, 135@NCs, 150@NCs, and 170@NCs, respectively. The NCs were then isolated from the crude solution by centrifugation at 3000 rpm for 5 minutes, followed by re-dispersion in hexane. For $CsPbI_3$ NCs, there is a controversial argument regarding the use of antisolvent (*e.g.* methyl acetate, MeOAc), since some reports found that the addition of MeOAc in the crude solution could accelerate the degradation of as-formed $CsPbI_3$ NCs into a yellow orthorhombic phase.[15] In our case, we also observed the fast degradation of $CsPbI_3$ NCs when MeOAc was used, even with the tuned volume ratio between added antisolvent and crude solution in a commonly reported range of 1 : 3–3 : 1 (see Experimental section). Therefore, in this work, we focused on antisolvent-free isolation of the NCs.

2.1. Compositional and morphological analysis of as-synthesized $CsPbI_3$ NCs

To verify if any immediate compositional change occurs in PNC thin film surfaces for the $CsPbI_3$ NCs synthesized at different temperatures, we first performed X-ray photoelectron spectroscopy (XPS) characterization for as-synthesized samples. Only one chemical state was resolved for Cs (Cs 3d5/2 at 723.9 eV), Pb (Pb 4f7/2 at 137.8 eV), and I (I 3d5/2 at 618.3 eV) (Fig. S1 in ESI†). The binding energy values correspond to Cs^+, Pb^{2+}, and I^- as expected for $CsPbI_3$.[16,17] As shown in Table 1, the surface composition is close to $Cs_{0.5}Pb_{1.0}I_{2.6}$ for all the samples, which indicates depletion of both Cs and I at the surface compared to the theoretical stoichiometric bulk ratio of $CsPbI_3$. The desorption of I is partially induced by the X-ray and electron beam during the XPS measurements.[18] Most noteworthy, there was only negligible fluctuation among the samples synthesized at different temperatures. This confirms our assumption that the injection temperature does not alter the initial NC surface composition. The surface depletion of Cs has been previously observed for $CsPbI_3$ NCs and linked to the NC purification and subsequent ligand exchange process.[16] Oleylammonium halide ($OLAm^+X^-$) is considered as a capping layer since highly ionic $CsPbX_3$ NCs easily bind with ionic ligands,[19] which can partially replace Cs^+ cations on the surface of $CsPbI_3$ NCs. Pronounced segregation of Pb on the surface of halide perovskites has been associated with perovskite degradation.[20] However, the peak fitting of the XPS spectra (Fig. S1†) does not hint to any degradation process, as the formation of Pb^0 (with binding energies at 136.9 eV and 141.3 eV)[21,22] was not detected. As for 120@NCs, the nearly instantaneous degradation of NC films prevented us from collecting any reliable XPS data.

To evaluate the phase purity of the target NCs upon the injection temperature tuning, we recorded XRD patterns on as-formed films of 135@NCs, 150@NCs, and 170@NCs (Fig. 1a–c). We performed Rietveld fitting on these XRD patterns and found that all the NCs crystallize in the orthorhombic γ-$CsPbI_3$ (black) phase (space group is *Pnam*). The refined crystal structure of the NCs is shown in Fig. 1d. The desired very low goodness-of-fit (χ^2) and residual weighing factor (R_{wp}) (see Tables S1 and S2 in ESI† for the detailed refinement parameters), achieved when employing only γ-$CsPbI_3$ phase patterns, confirms the high phase purity of the as-synthesized $CsPbI_3$ NCs, and highlights the reliability of the refined structural parameters. The 120@NCs sample is an exception showing additional strong signals in its XRD pattern (Fig. 1e), which correspond the orthorhombic (yellow)

Table 1 X-ray photoelectron spectroscopy (XPS) analysis (atomic ratios normalized to Pb = I) for 135@NCs, 150@NCs, and 170@NCs

Element	135@NCs	150@NCs	170@NCs
Cs	0.52	0.50	0.54
Pb	1.00	1.00	1.00
I	2.59	2.52	2.65

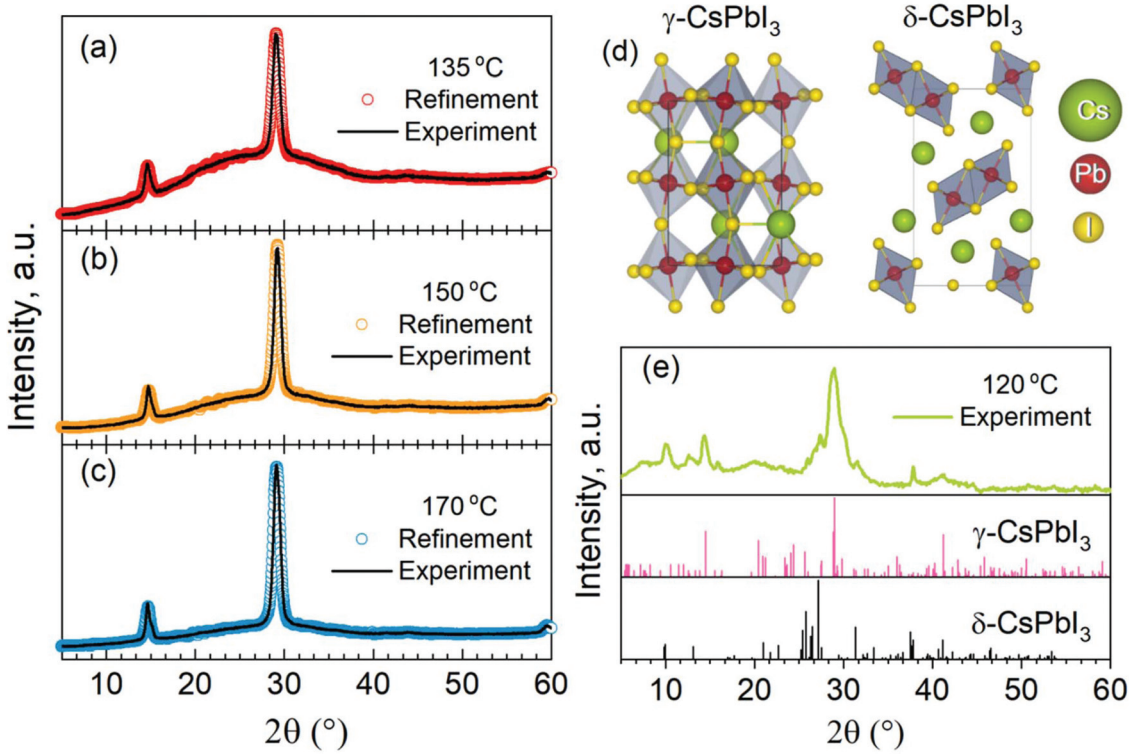

Fig. 1 (a–c) Experimental (open circles) and refined (solid lines) profiles obtained after the full-pattern Rietveld refinement of the XRD patterns of 135@NCs, 150@NCs, and 170@NCs. (d) The refined crystal structure of orthorhombic (black) γ-$CsPbI_3$ NCs and the crystal structure of orthorhombic (yellow) δ-$CsPbI_3$. (e) The XRD pattern of 120@NCs along with the γ-$CsPbI_3$ (obtained from the refinement) and δ-$CsPbI_3$ reference (reference code: 01-084-2969) XRD patterns.

δ-$CsPbI_3$ (Fig. 1d). This observation is in good consistency with a previous report showing the formation of $CsPbI_3$ nanorods in the yellow phase at the injection temperature of 120 °C.[23]

The morphology of $CsPbI_3$ NCs formed at different injection temperatures was evaluated by TEM measurements. Fig. 2a–c show the shape and size evolution of $CsPbI_3$ NCs with average diameters of 9.3 ± 0.6 nm (135@NCs), 9.4 ± 0.4 nm (150@NCs), and 9.5 ± 0.3 nm (170@NCs), which are consistent with the reported sizes (about 9–10 nm) for $CsPbI_3$ nanocubes.[24] The TEM images of 120@NCs are not reported due to their fast phase degradation (Fig. 1e). A small amount of nanorods are formed for 135@NCs (Fig. 2a), suggesting that low temperatures (<135 °C) can initiate the growth of one-dimensional (1D) nanocrystals, which has also been reported earlier for $CsPbX_3$ [25,26] and for $CsPbI_3$ [23] in particular. The high-resolution TEM (HRTEM) images in Fig. 2a–c show that all the $CsPbI_3$ NCs exhibit high crystallinity and their lattice spacing values in the (114) direction lie within 2.75–2.81 Å.

2.2. Optical properties of as-synthesized $CsPbI_3$ NCs

Fig. 3a shows the absorption spectra of $CsPbI_3$ NC colloidal dispersions right after the synthesis at the tuned reaction temperatures between 135 and 170 °C. When moving from 135 °C to 170 °C, a minor red-shift of the first exciton peak wavelength is detected. The Tauc plot analysis (Fig. 3b) confirms that E_g of the as-formed NCs slightly decreases with the increase in the injection temperature from 135 °C to 170 °C, showing a nearly negligible change in E_g (see Table 2). This trend is consistent with the TEM study, in which a very small size change (*e.g.* 9.3–9.5 nm) within the tuned temperature window (135–170 °C) is detected. Fig. 3c compares the PL spectra of these $CsPbI_3$ NC dispersions. The PL main peak position of 135@NCs, centered at ~684 nm, is almost identical to those of 150@NCs and 170@NCs, which is assigned to the majority of as-formed nanocubes. A secondary PL band at about 625 nm is observed for 135@NCs, attributed to the formation of small amount of nanorods (see Fig. 2a) at this temperature, which has also been observed for $CsPbX_3$ (X = I, Br, Cl).[23,25,26] The PLQY is as high as 96, 93, and 73% for 135@NCs, 150@NCs, and 170@NCs, respectively. We attribute the highest PLQY of 96% for 135@NCs to their longest excited state lifetime, as will be detailed in following section. Note that this (96%) is one of the highest PLQY among all the reported values for pristine $CsPbI_3$ NCs (which are typically below 90%[28–30]). All the samples exhibit narrow emission bands, indicating that the size distribution of as-formed NCs can be precisely controlled. The full width at half maximum (FWHM) values of the PL spectra lie in the range of 35–37 nm (Table 2). The PL spectrum of 135@NCs was deconvoluted

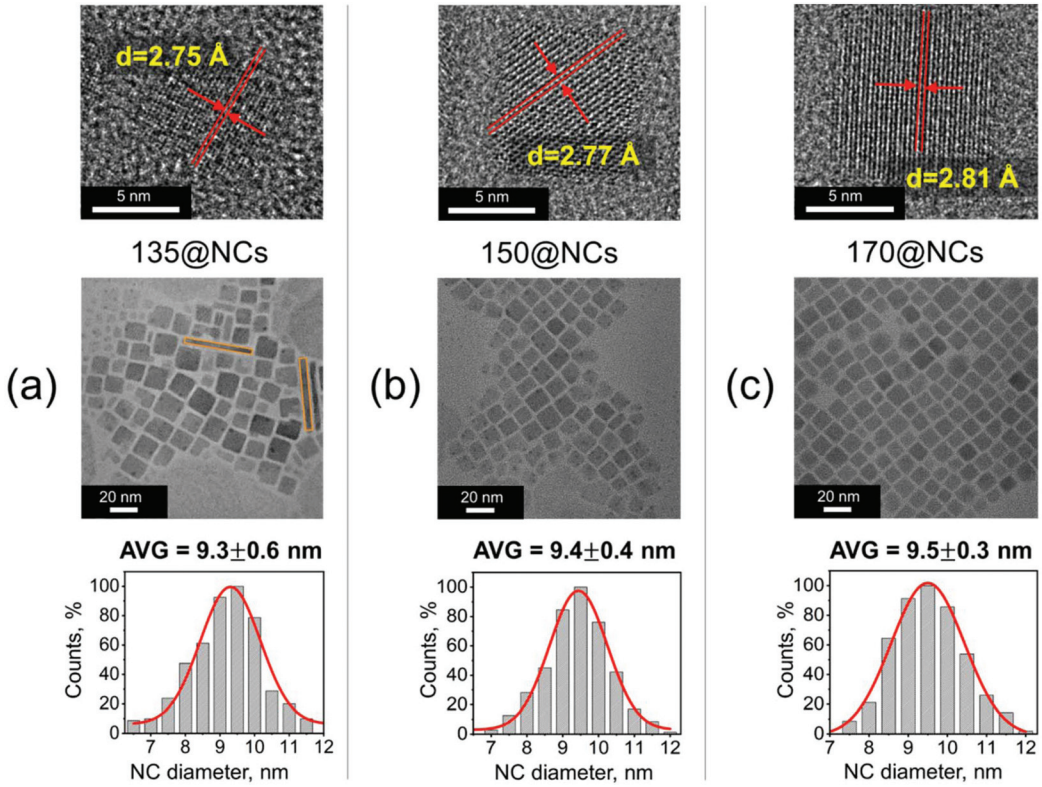

Fig. 2 Transmission electron microscopy (TEM) images of (a) 135@NCs, (b) 150@NCs, and (c) 170@NCs. HRTEM images of a single $CsPbI_3$ NC are also presented in the top part of each figure (a–c) with respective lattice spacing value, which corresponds to (114) planes of $CsPbI_3$. The size distribution histogram of the particles is presented in the bottom part of each figure (a–c), indicating average diameters of 9.3 ± 0.6 nm (135@NCs), 9.4 ± 0.4 nm (150@NCs), and 9.5 ± 0.3 nm (170@NCs), respectively. In (a), the observed nanorods are highlighted with orange lines. The black spots present on the NCs have been attributed to the electron beam-induced nucleation of Pb^0 NCs on $CsPbI_3$ NCs.[27]

with two Gaussian peaks centered at 629 and 684 nm (see Fig. S2b†) for the determination of the FWHM values. The relationship between the optical properties of the as-synthesized $CsPbI_3$ NCs and their injection temperatures is summarized in Table 2.

To clarify the influence of injection temperature on the PL dynamics of as-formed $CsPbI_3$ NCs, time-resolved PL (TRPL) measurements were conducted for the NC dispersions. Fig. 3d compares the PL decays of the as-formed NCs synthesized at different temperatures. All the decays can be well fitted with a bi-exponential function and the fitting results are summarized in Table S3.† We assign the fast component to the trap-assisted nonradiative recombination and the slow component to the intrinsic recombination (*i.e.* radiative recombination), respectively.[31,32] The decays of the NCs formed at 135–170 °C (135@NCs, 150@NCs, and 170@NCs) show similar lifetimes (*i.e.* 18.5–23.0 ns) of the fast component, implying that the number of surface traps is comparable in these three as-synthesized samples. Interestingly, the 135@NC sample demonstrates a relatively long radiative lifetime (58.2 ns) compared to that of the other two NCs (50.1 and 47.0 ns), leading to the highest PLQY (96%) as previously observed. This may suggest that the 135@NCs have the least number of mid-gap energy states, elongating the band edge recombination process.[33]

2.3. Influence of injection temperature on optical, structural, and morphological stabilities of $CsPbI_3$ NCs

The influence of injection temperature on the stabilities of $CsPbI_3$ NCs was evaluated through a holistic stability investigation for $CsPbI_3$ NCs in dispersion and films by combining a thorough optical, XRD, and TEM characterization as a function of storage time. The dispersions and films of the targeted $CsPbI_3$ NCs (synthesized at different injection temperatures) were stored under ambient conditions (in dark, RH ~ 40%, T = 25 °C) before and in-between the measurements.

The preservation of the original black phase of $CsPbI_3$ perovskite is the key to high-performance NCs-based devices. Therefore, we assessed the phase stability of the NCs in terms of the transition from the black (γ-orthorhombic) to the yellow (δ-orthorhombic) phase. The latter is characterized by disappearance of the absorption feature (*e.g.* absorption onset and first exciton peak) and the quenching of the PL intensity.[5]

Fig. S2–S4† show the temporal evolution of the absorption and PL spectra of the three $CsPbI_3$ NC samples. The 150@NCs sample displays nearly unchanged absorption and PL intensities up to 12 weeks of air storage (Fig. S3†). This suggests that the NCs formed at the injection temperature of 150 °C are very stable as they retain their initial black phase despite being

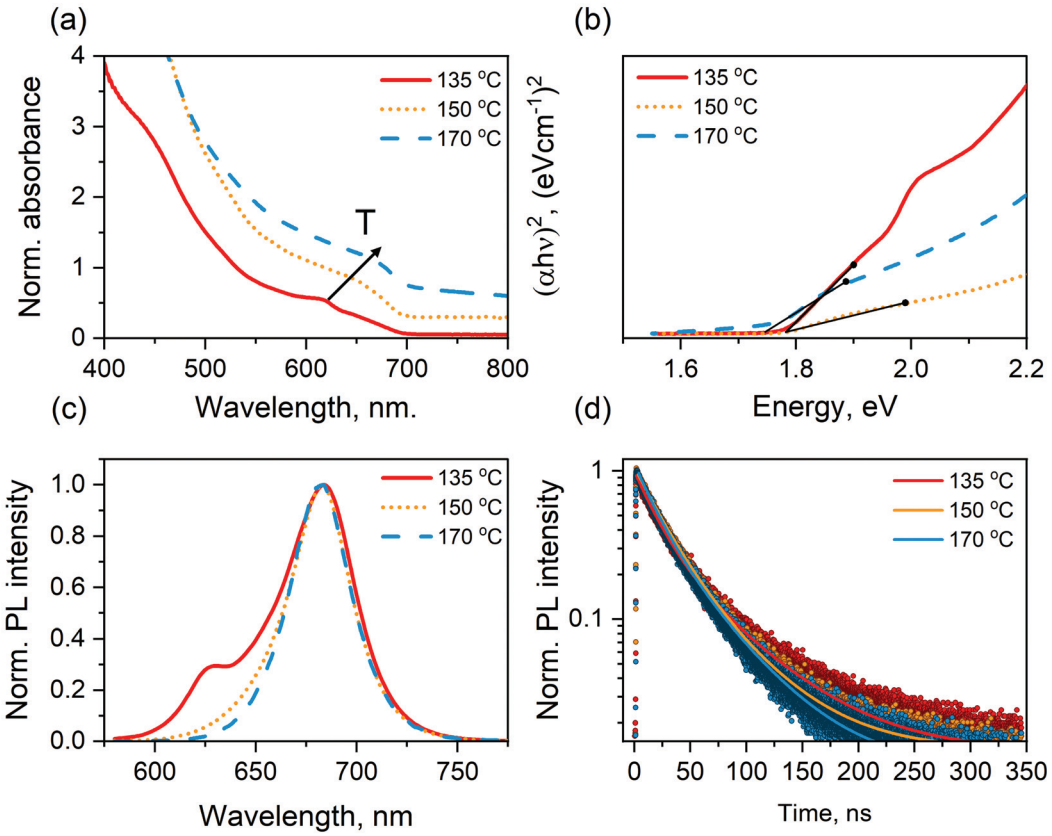

Fig. 3 (a) Absorption spectra, (b) Tauc plot analysis, (c) normalized PL spectra, and (d) time-resolved PL (TRPL) decays of as-prepared $CsPbI_3$ NCs dispersions formed at 135 °C, 150 °C, and 170 °C (samples 135@NCs, 150@NCs, and 170@NCs).

Table 2 Optical properties of as-synthesized $CsPbI_3$ NCs

Sample	Absorption exciton peak position, nm	Band gap (E_g), eV	PL peak position (s), nm	FWHM, nm	PLQY (%)
135@NCs	668	1.78	629, 684	37, 36	96
150@NCs	652	1.78	683	35	93
170@NCs	668	1.75	684	36	73

exposed to air (*i.e.* in the presence of moisture and oxygen). The absorption and PL spectra of 170@NCs sample (Fig. S4†) undergo a small red shift, which is also observed for 135@NCs (main emission peak centered at 684 nm) (Fig. S2†). We attribute the red-shift (Stokes shift) in PL spectra to the formation of large size of irregular nanoparticles due to the gradual phase aggregation,[31] evidenced by the following morphological stability study. However, the major optical features in the case of 170@NCs are still retained after 69 days of storage, demonstrating much longer stability compared to those of commonly reported $CsPbI_3$ NCs formed at this temperature (170 °C).[6]

The absorption spectra of 135@NCs sample turn out to be more and more scattered, which indicates a gradual loss in their absorption onset features, and, hence the material degradation. Together with a slight phase aggregation induced red-shift of the main PL peak (originally centered at 684 nm) which is similar to the case of 170@NCs, the disappearance of the secondary PL peak (originally centered at 629 nm) is observed after 18 days, due to the decomposition of unstable nanorods formed at this temperature (135 °C).[34] Fig. 4 shows the variation of integrated PL intensity corrected with the absorption at the excitation wavelength (namely relative PLQY) as a function of the storage time of the targeted $CsPbI_3$ NC dispersions. During 14 weeks of storage in air, the 150@NCs sample shows a nearly unchanged PL intensity, while for 170@NCs and 135@NCs samples it declined to about 76% and 15% of their respective initial values.

The stability of PL dynamics was further analyzed by measuring the evolution of the TRPL over a total period of 9 weeks for each NC dispersion (Fig. S5†). The 150@NCs sample shows a constant PL decay behavior after 9 weeks of air storage, which is in good agreement with their stable PL intensity during a similar storage period. Compared to the case of 150@NCs, the 170@NCs sample shows a slightly faster decay, while the decay lifetime of 135@NCs sample is shortened to nearly half of the initial value for both fast and slow components after 9 weeks in air. Based on the above-discussed optical and photophysical stability studies, we conclude that 150@NCs dispersions indeed display the highest stability compared to those formed at more commonly reported injection

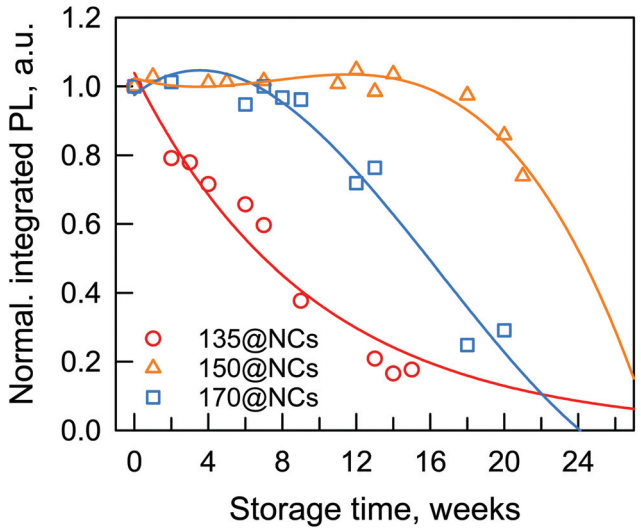

Fig. 4 PL trends for the $CsPbI_3$ NCs synthesized at the targeted injection temperatures. The integrated normalized PL intensity *vs.* the storage time (weeks) is reported. $CsPbI_3$ NC dispersions were stored in dark under ambient conditions (RH ~ 40%, T = 25 °C) between each measurement. Solid lines are guides to the eye.

temperatures (*e.g.* 170 °C). In addition, low injection temperatures (*e.g.* 135 °C) are detrimental to the optical stability of the resulting NC dispersions.

It is well-known that the NC films are more prone to degradation than their colloidal counterparts due to the weaker protective abilities of the ligands in the solid state.[35] Nevertheless, studies on films are essential to screen the potential of these materials for real optoelectronic applications, such as photovoltaics. Therefore, we examined the stability of NC films to gain insights on the degradation of their corresponding solar cells (see section 2.4).

We firstly identified the phase transition of the NC films by XRD analysis. In general, in addition to the featured peaks at around 28.7° and 14.3° for an indication of the black phase, several peaks (*e.g.* ~8°, ~27°, and ~31°) that are corresponding to the yellow phase gradually appear in the XRD patterns of the NC films (Fig. 5a–c). It is clearly observed that the 150@NCs sample retains the long-lived photoactive (black) phase, with no traces of orthorhombic (yellow) phase in their XRD patterns up to 33 days (Fig. 5b). With respect to the other samples, the first sign of degradation was detected on day 10

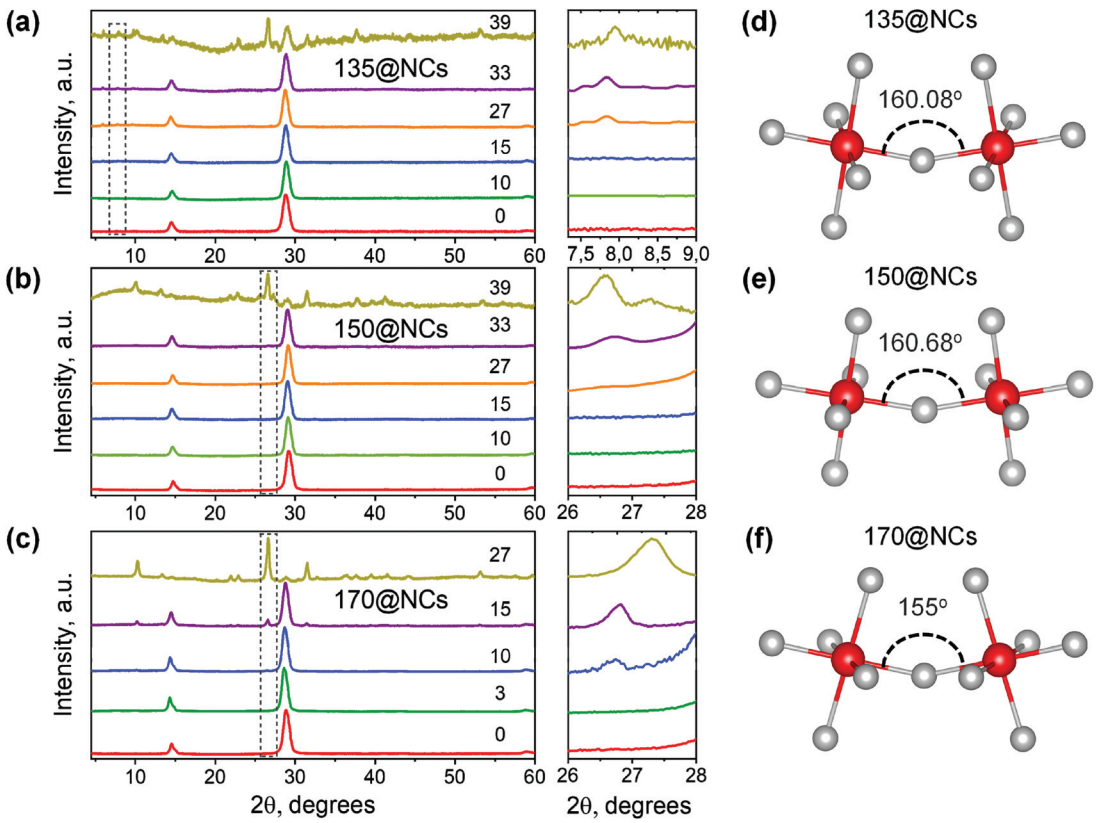

Fig. 5 (a–c) Storage time-dependent XRD patterns of $CsPbI_3$ NC films synthesized at 135 °C, 150 °C, and 170 °C (135@NCs, 150@NCs, and 170@NCs). Selected 2θ range (26 to 28° and 7.5 to 9°) of the XRD patterns are presented to highlight the evolution of peaks related to δ-$CsPbI_3$ phase. The NC films fully converted into δ-$CsPbI_3$ on day 39 (135@NCs and 150@NCs) and day 27 (170@NCs). The numbers in panels (a–c) represent the number of days. Day 3 is not represented for the 135@NCs and 150@NCs samples since no visible change has occurred. (d–f) The portrayal of Pb–I–Pb dihedral angles in the crystal structures of 135@NCs (160.08(5)°), 150@NCs (160.68(7)°), and 170@NCs (155.00(2)°). The angles were extracted from the full pattern fitting of X-ray diffraction patterns. The numbers in parentheses of the dihedral angle values are the estimated standard deviations of the last significant figure.

and day 27 for 170@NCs and 135@NCs, respectively, as shown in Fig. 5c and a. The XRD pattern of the as-synthesized 120@NCs sample clearly shows an intense signal from the orthorhombic phase even in its fresh form (Fig. 1e), therefore this sample was not monitored further. Overall, the XRD analysis indicates that the 150@NCs and 120@NCs samples are the most and least phase stable NCs, respectively. The highest structural stability of 150@NCs is consistent with their most stable optical properties discussed above.

To evaluate the photostability of the as-synthesized $CsPbI_3$ NCs, we have conducted the stability experiment for the NC films under indoor light exposure for the most (150@NCs) and the least (170@NCs) stable samples. The NCs film samples were prepared similarly as for the other characterizations (as described in Experimental section) and were kept under continuous room light exposure for the 3 days (light intensity: 1460 lux) without any protection. As expected, the samples have shown a much quicker degradation in such harsh conditions. Based on the XRD study (Fig. S6†), we can conclude that 150@NCs still mainly preserve the black phase after 3 days, while 170@NCs transformed to the yellow phase. These results show that 150@NCs exhibit the highest phase stability also under continuous illumination.

The size of the cubooctahedral voids of γ-$CsPbI_3$ does not match that of Cs^+ (A-site) ions, which creates extra space around the PbI_6 octahedra in the lattice. As a result, the PbI_6 octahedra rotate and tilt around the Cs^+ ions, thus minimizing the free space. The gradual tilting of the octahedra of the 3D γ-$CsPbI_3$ eventually transforms the material into 1D δ-$CsPbI_3$ at room temperature.[36] The higher the initial distortion of the octahedra in the as-formed NCs, the faster the transformation (structural deformation). The extent of the distortion scales inversely with the Pb–I–Pb dihedral angle of the $CsPbI_3$ structure; a smaller angle means a higher octahedral distortion. Fig. 5d–f depicts the Pb–I–Pb dihedral angles (obtained from their structural refinement) between the octahedra of 135@NCs, 150@NCs, and 170@NCs. The 150@NCs sample shows the largest dihedral angle of 160.68°, which establishes its higher crystal (phase) stability (up to 33 days) among the three samples. On the other hand, the accelerated degradation (started already on day 10) of 170@NCs can be attributed to the smallest Pb–I–Pb angle (155°) and, hence, the higher octahedral distortion. The distortion angle (and so the crystal stability) in the 135@NCs is slightly smaller compared to in the 150@NCs.

We have also calculated the distortion index (D) from the structural refinement data (Table S1†). This indicates the normalized deviation from the average bond length and positional disorder parameter of Pb and I atoms within the single octahedron (Fig. S7†). The 150@NCs sample has the lowest D value (1.3%) than the other two samples (D = 4–8%), which suggests a lower distortion of the individual octahedron. Therefore, the 150@NCs sample has overall the highest crystal symmetry (lowest octahedral distortion and lowest distortion of individual octahedron) among the three samples, which suggests that the injection temperature of 150 °C ensures the highest formation energy for the structural distortion of $CsPbI_3$ NCs and decelerates their phase transformation.

The morphological stability of $CsPbI_3$ NCs formed at 135–170 °C were assessed by collecting TEM images at different aging times, as shown in Fig. S8.† It is clearly observed that all the as-prepared samples featured a symmetric square shape with a well monodispersed pattern. After 1 week of storage under ambient conditions, irregularly-shaped nanoparticles were formed for the 135@NCs and 170@NCs samples, due to a known ligands-induced aggregation effect.[31] Gradually, these nanoclusters increased in size up to week 2. On the other hand, most of the nanocubes of 150@NCs sample still retain their original square shape and size. We even observed the so-called lateral fusion effect[37] for both 135@NCs and 170@NCs samples (see Fig. S6j and S6l,† respectively), while the 150@NCs sample (Fig. S6k†) surprisingly did not show any obvious degradation signs after five weeks of storage. This suggests that the $CsPbI_3$ NCs formed at 150 °C indeed exhibit the highest morphological stability, which contributes to their strongest resistance to moisture penetration compared to the NCs formed at the other examined temperatures.

2.4. Stability of planar n-i-p solar cells with $CsPbI_3$ NC light-harvesters

After assessing the optical, structural, and morphological stabilities of $CsPbI_3$ NCs in dispersion and/or film form, we deepened our investigation by developing n-i-p planar PSCs with NCs as the light absorber. Our ultimate goal was to correlate the device stability (shelf storage conditions) with the temperature (135, 150, or 170 °C) at which $CsPbI_3$ NCs are synthesized. To the best of our knowledge, a similar correlation between the device performance and the injection temperature has not previously been elucidated. Nevertheless, it is paramount to understand how to address the key weakness of perovskite NC solar cells, *i.e.* their modest stability.

In this work, we fabricated proof-of-concept devices with 'FTO/c-TiO_2/$CsPbI_3$ NCs/spiro-OMeTAD/Au' structure (see Experimental section). It is worth noting that this work did not aim to maximize the power conversion efficiency by optimizing the thickness of each layer or other parameters but rather focused on improvements of the device stability in relation to the perovskite NC synthesis.

The current density (J)–voltage (V) curves of the best-performing PSCs are shown in Fig. S9† and the key photovoltaic parameters are summarized in Fig. S10.† Devices based on 150@NCs exhibit the highest PCE (3.0%) compared to other cells employing the NCs synthesized at 135 and 170 °C. This is mainly attributed to the enhancement of both short-circuit current density (J_{SC}) and open-circuit voltage (V_{OC}) in the case of 150@NCs (Fig. S10†). After the fabrication, the unencapsulated PSCs were stored in dry air (RH ≤ 10%) in dark and J–V curves were periodically recorded over a total period of 26 days in order to determine the shelf-lifetime of the devices. Fig. 6 compares the trend of the normalized PCEs over time for the $CsPbI_3$ NCs-based devices with different injection tempera-

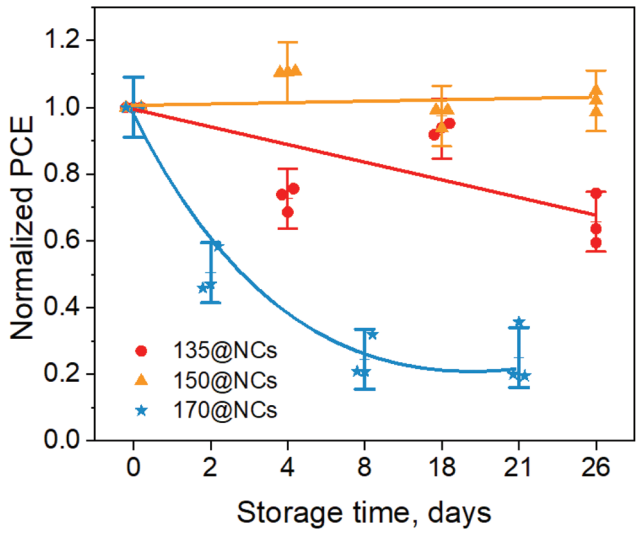

Fig. 6 Stability of unencapsulated PSCs with 135@NCs, 150@NCs, or 170@NCs as the absorber layer. PSCs were stored in dry air. The performance of three devices per each case is reported. Solid lines are guides to the eye.

tures. In the figure, 3 devices have reported for each case for statistic evaluation. It is evident that the 150@NCs-based devices exhibit unchanged performance upon 26 days of shelf storage in dry air. Conversely, after the same time span of 26 days only 60% and nearly 20% of the initial PCE is retained for 135@NCs- and 170@NCs-based devices, respectively. Storage time-dependent photovoltaic parameters for $CsPbI_3$ NCs-based solar cells with different injection temperatures (135–170 °C) are summarized in Table S4.† The highest device stability was achieved when employing $CsPbI_3$ NCs formed at 150 °C, in good agreement with their outstanding optical and structural stabilities. It is noteworthy that the monitoring period (up to 26 days) for the device stability in this work is much longer than those reported for similar types of $CsPbI_3$ NCs-based solar cells (usually up to 10 days).[16] This confirms the great stability of the NCs formed at 150 °C achieved in this work. In addition, we note that the degradation rates for 135@NCs and 170@NCs are reversed between film (*e.g.* XRD studies and solar cells) and suspension (*e.g.* PL and TRPL measurements in hexane) phases. It is known that colloidal perovskite NCs can be better protected against the penetration of oxygen and moisture in a non-polar solvent (such as toluene or hexane) rather than in film phase, which is directly exposed to air.[38] Therefore, we speculate that the initial dihedral angle, *i.e.* the distortion factor, dominates the stability of $CsPbI_3$ NC films without the protection provided by the non-polar solvent. Hence, in this case a faster degradation rate of 170@NCs compared to that of 135@NCs was observed. On the other hand, from a crystal structure point of view, it is reported that a small lattice difference (*e.g.* 0.16 Å) can already induce a big change in the so-called surface adsorption energy (*ca.* 4 eV), as reported for other types of nanomaterials, such as Au nanoparticles.[39] In particular, a larger lattice distance corresponds to a lower surface adsorption energy. In our case, 170@NCs show slightly larger lattice distance (2.81 Å) that that (2.75 Å) of 135@NCs (see Fig. 2), which may result in a relatively lower adsorption rate of oxygen and moisture onto the NC surface. In suspension phase, we in turn attribute the faster degradation rate of 135@NCs compared to that of 170@NCs to their higher adsorption energy and, thus, to the higher initial surface trap density, which mostly influences the degradation rate when there is the protection from a non-polar solvent. Nevertheless, the 150@NCs sample is always the most stable among the three samples (135@NCs, 150@NCs, and 170@NCs) in both suspension and film forms, whose degradation rate is dominated by the distortion degree of the PbI_6 octahedra.

3. Conclusions

In summary, we have tuned the hot-injection reaction temperature of $CsPbI_3$ NCs in the range of 120–170 °C, which lies below the typically reported temperatures (*i.e.* 160–180 °C) for the formation of $CsPbI_3$ NCs. We show that $CsPbI_3$ NCs formed at 150 °C injection temperature (150@NCs) exhibit the highest phase stability, as demonstrated by the monitored changes in the optical, photophysical, structural, and morphological properties of dispersions and films over time. The transition from the 3D black (γ-orthorhombic) to the 1D yellow (δ-orthorhombic) phase of 150@NCs occurs after 33 days of storage under ambient conditions. The higher stability of this sample with respect to the others (synthesized at different injection temperatures) is induced by the lowest distortion of PbI_6 octahedra in the 150@NCs sample. The absence of phase transition from the black emitting to the yellow non-emitting phase of 150@NCs for over 1 month is also reflected in the notable stability of the corresponding 150@NCs-based solar cells, which display unchanged performance upon 26 days of shelf storage in dry air. Our findings highlight the possibility of developing $CsPbI_3$ NCs with competitive phase stability by a simple modification of the well-established synthesis protocol, without recurring to sophisticated ligands, compositional, or doping engineering approaches. We envision that this strategy could also help to enhance the stability of perovskite NCs with different compositions. Finally, this study demonstrates that there is a high need of performing holistic studies of the phase stability, even for heavily investigated materials like $CsPbI_3$, to boost the stability of corresponding optoelectronic devices.

4. Experimental section

4.1. Chemicals

Cs_2CO_3 (99.9%), octadecene (ODE, 90%), oleic acid (OA, 90%), oleylamine (OlAm, technical grade, 70%), lead(II) iodide (PbI_2, 99%), hexane (≥95%), methyl acetate (MeOAc, anhydrous), ethyl acetate (EA, 97%), titanium diisopropoxide bis(acetylacetonate) (TDBA, 75 wt% in isopropanol), bis(trifluoro-

methane)sulfonimide lithium salt (Li-TFSI, 99.95%), chlorobenzene (extra dry, 99.8%), acetonitrile (99.9%), and 4-*tert*-butyilpyridine (4-*t*BP) were purchased from Sigma-Aldrich. 2,2′,7,7′-Tetrakis[*N*,*N*-di(4-methoxyphenyl)amino]-9,9′-spirobifluorene (Spiro-OMeTAD, 99%) and tris[2-(1*H*-pyrazol-1-yl)-4-*tert*-butylpyridine]cobalt(III)tri[bis-(trifluoromethane) sulfonimide] (FK209, >98%) were purchased from Lumtec and Dyenamo, respectively. All chemicals were used without further purification.

4.2. Preparation of Cs-oleate

Cs_2CO_3 (407.3 mg) was loaded into a 50 mL three-neck flask along with ODE (15 mL) and OA (1.25 mL), purged 3 cycle times in between argon (Ar) and vacuum atmosphere at room temperature (RT) prior to heating up to 120 °C. When the temperature reached 120 °C, an addition (0.25 ml) of OA was injected in the Cs-based precursor to ensure a good solubility of Cs_2CO_3 in ODE. The mixed precursor was degassed under vacuum for 2.5 hours at 120 °C, and then kept under Ar at the same temperature until all Cs_2CO_3 was dissolved by showing a transparent solution as a sign of Cs-oleate formation.

4.3. Synthesis of $CsPbI_3$ nanocrystals

$CsPbI_3$ NCs were synthesized following a well-known protocol by Protesescu *et al.*[8] with some minor adaptations. In a typical synthesis, PbI_2 (216.7 mg) was loaded into a 25 mL three-neck flask along with ODE (12.5 ml), OA (1.25 mL) and OlAm (1.25 mL), purged 3 cycle times in between Ar and vacuum atmosphere at RT prior to heating up to 120 °C. The halide precursor was degassed under vacuum for 2.5 hours at 120 °C. Then, the temperature was kept at 120 °C or increased to desired temperatures (*e.g.* 135 °C, 150 °C and 170 °C) under Ar, and 0.8 mL of as-prepared Cs-oleate solution (~0.121 mM) was swiftly injected under vigorous stirring. The color of the solution instantaneously turned from transparent yellow to red (from bright to dark red depending on the temperature), exhibiting the formation of nanocrystals. The reaction was kept at the injection temperature for 10 s before an ice-water bath was set under the three-neck flask to quench the further growth of nanocrystals. The crude solution was either purified with an addition of MeOAc in a volume ratio of 1 : 3–3 : 1 and centrifuged at 8000 rpm for 5 min, or directly centrifuged at 3000 rpm for 5 min without adding any antisolvent. After discarding the supernatant, the remaining NC precipitation was fully dried in a nitrogen-filled glovebox and then redispersed in hexane before further usage.

4.4. Fabrication of $CsPbI_3$ NCs-based PSCs with n-i-p planar structure

FTO glass substrates (Greatcell Solar, TEC 15), 20 mm × 20 mm, were chemically etched with 2 M HCl aqueous solution and zinc powder. The etched FTO substrates were then sonicated using an aqueous solution of Hellmanex III solution (2%), DI water, acetone, and 2-propanol for 15 min in each step, successively. The substrates were then treated with UV-ozone for 15 min to remove organic residuals and increase hydrophilicity. A 30 nm thick compact TiO_2 layer (c-TiO_2) was deposited on the as-prepared patterned substrate by spray pyrolysis of 0.38 M TDBA solution in 2-propanol at 450 °C. The films were then sintered at 450 °C for 1 h in air. An active layer of $CsPbI_3$ NCs was deposited on as-prepared c-TiO_2 layers *via* layer-by-layer spin-coating under ambient conditions (RH ~ 40%, 25 °C). A 70 mg ml^{-1} of $CsPbI_3$ NCs solution in hexane was sonicated for 5 min before conducting a two-step spin-coating program (1000 rpm for 30 s and 2000 rpm for 45 s). To produce uniform NCs film, 30 μl of NCs solution was firstly dropped on the surface immediately followed by spinning at 1000 rpm for 30 s. Once the speed reached to 2000 rpm, 300 μl EA was swiftly injected on the surface of spinning NCs film. These steps were repeated 6 times to obtain the film with a desired thickness (~200 nm). As-prepared NCs film coated substrates were immediately transferred to a glovebox and a spiro-OMeTAD layer was spin-coated on top of the NCs film at 1800 rpm for 30 s. The spiro-OMeTAD solution was made by adding 36.2 mg spiro-OMeTAD to 1 ml chlorobenzene, 14.4 μl 4-*t*BP, 8.7 μl Li–TFSI (520 mg ml^{-1}), and 14.5 μl FK209 (300 mg ml^{-1}) were used as dopants. The films were transferred to the dry box overnight to ensure the spiro-OMeTAD doping process. Finally, 75 nm thick gold contact was thermally evaporated on top of the spiro-OMeTAD layer to form the back contact. Evaporation was conducted in a high vacuum (6×10^{-6} mbar).

Author contributions

The manuscript was written through contributions of all authors. All authors have given approval to the final version of the manuscript. A. M.: Data curation, methodology, formal analysis, writing – original draft; G. K. G.: Data curation, formal analysis, writing – review & editing; M. L.: Methodology, data curation, formal analysis, investigation, writing – review & editing; J.-H. S.: Formal analysis, writing – review & editing; N. S. M. V.: Formal analysis, writing – review & editing; H. A.-L.: Data curation, formal analysis, writing – review & editing; K. L.: Data curation, formal analysis, writing – review & editing; P. V.: Conceptualization, funding acquisition, project administration, validation, visualization, writing – review & editing.

Conflicts of interest

The authors declare no competing financial interests.

Acknowledgements

Dr Mari Honkanen and Tampere Microscopy Center are gratefully acknowledged for the TEM images. The authors also thank Dr Antti Tukiainen for his support with the solar cell measurements. This work is part of the Academy of Finland Flagship Programme, Photonics Research and Innovation (PREIN), Decision No 320165. A. M. and P. V. thank the finan-

cial support of Tampere University, Faculty of Engineering and Natural Sciences. M. L. thanks Finnish Cultural Foundation (00210670) for funding. J.-H. S. thanks Academy of Finland (project 308307). P. V. and J.-H. S. also acknowledge the support of Jane & Aatos Erkko foundation (project 'ASPIRE').

References

1 F. Ke, C. Wang, C. Jia, N. R. Wolf, J. Yan, S. Niu, T. P. Devereaux, H. I. Karunadasa, W. L. Mao and Y. Lin, *Nat. Commun.*, 2021, **12**, 1–8.
2 A. Marronnier, G. Roma, S. Boyer-Richard, L. Pedesseau, J.-M. Jancu, Y. Bonnassieux, C. Katan, C. C. Stoumpos, M. G. Kanatzidis and J. Even, *ACS Nano*, 2018, **12**, 3477–3486.
3 R. J. Sutton, M. R. Filip, A. A. Haghighirad, N. Sakai, B. Wenger, F. Giustino and H. J. Snaith, *ACS Energy Lett.*, 2018, **3**, 1787–1794.
4 A. Dutta and N. Pradhan, *ACS Energy Lett.*, 2019, **4**, 709–719.
5 A. Swarnkar, A. R. Marshall, E. M. Sanehira, B. D. Chernomordik, D. T. Moore, J. A. Christians, T. Chakrabarti and J. M. Luther, *Science*, 2016, **354**, 92–95.
6 J. Shamsi, A. S. Urban, M. Imran, L. De Trizio and L. Manna, *Chem. Rev.*, 2019, **119**, 3296–3348.
7 Y. Hu, F. Bai, X. Liu, Q. Ji, X. Miao, T. Qiu and S. Zhang, *ACS Energy Lett.*, 2017, **2**, 2219–2227.
8 L. Protesescu, S. Yakunin, S. Kumar, J. Bär, F. Bertolotti, N. Masciocchi, A. Guagliardi, M. Grotevent, I. Shorubalko, M. I. Bodnarchuk, C.-J. Shih and M. V. Kovalenko, *ACS Nano*, 2017, **11**, 3119–3134.
9 Q. A. Akkerman, D. Meggiolaro, Z. Dang, F. De Angelis and L. Manna, *ACS Energy Lett.*, 2017, **2**, 2183–2186.
10 X. Shen, Y. Zhang, S. V. Kershaw, T. Li, C. Wang, X. Zhang, W. Wang, D. Li, Y. Wang, M. Lu, L. Zhang, C. Sun, D. Zhao, G. Qin, X. Bai, W. W. Yu and A. L. Rogach, *Nano Lett.*, 2019, **19**, 1552–1559.
11 F. Liu, Y. Zhang, C. Ding, S. Kobayashi, T. Izuishi, N. Nakazawa, T. Toyoda, T. Ohta, S. Hayase, T. Minemoto, K. Yoshino, S. Dai and Q. Shen, *ACS Nano*, 2017, **11**, 10373–10383.
12 Y. Wang, X. Liu, T. Zhang, X. Wang, M. Kan, J. Shi and Y. Zhao, *Angew. Chem., Int. Ed.*, 2019, **58**, 16691–16696.
13 R. X. Yang and L. Z. Tan, *J. Chem. Phys.*, 2020, **152**, 034702.
14 A. Dutta, S. K. Dutta, S. Das Adhikari and N. Pradhan, *Angew. Chem., Int. Ed.*, 2018, **57**, 9083–9087.
15 Y. Zhang, T. D. Siegler, C. J. Thomas, M. K. Abney, T. Shah, A. De Gorostiza, R. M. Greene and B. A. Korgel, *Chem. Mater.*, 2020, **32**, 5410–5423.
16 X. Ling, S. Zhou, J. Yuan, J. Shi, Y. Qian, B. W. Larson, Q. Zhao, C. Qin, F. Li, G. Shi, C. Stewart, J. Hu, X. Zhang, J. M. Luther, S. Duhm and W. Ma, *Adv. Energy Mater.*, 2019, **9**, 1900721.
17 J. Kim, B. Koo, W. H. Kim, J. Choi, C. Choi, S. J. Lim, J. S. Lee, D. H. Kim, M. J. Ko and Y. Kim, *Nano Energy*, 2019, **66**, 104130.
18 Z. Dang, J. Shamsi, Q. A. Akkerman, M. Imran, G. Bertoni, R. Brescia and L. Manna, *ACS Omega*, 2017, **2**, 5660–5665.
19 J. De Roo, M. Ibáñez, P. Geiregat, G. Nedelcu, W. Walravens, J. Maes, J. C. Martins, I. Van Driessche, M. V. Kovalenko and Z. Hens, *ACS Nano*, 2016, **10**, 2071–2081.
20 N. Fernández-Delgado, M. Herrera, F. J. Delgado, A. H. Tavabi, M. Luysberg, R. E. Dunin-Borkowski, E. J. Juárez-Pérez, B. C. Hames, I. Mora-Sero, I. Suárez, J. P. Martinez-Pastor and S. I. Molina, *Nanotechnology*, 2019, **30**, 135701–135711.
21 G. Niu, W. Li, J. Li, X. Liang and L. Wang, *RSC Adv.*, 2017, **7**, 17473–17479.
22 M. Acik, I. K. Park, R. E. Koritala, G. Lee and R. A. Rosenberg, *J. Mater. Chem. A*, 2018, **6**, 1423–1442.
23 T. Yang, Y. Zheng, Z. Du, W. Liu, Z. Yang, F. Gao, L. Wang, K.-C. Chou, X. Hou and W. Yang, *ACS Nano*, 2018, **12**, 1611–1617.
24 Q. Zhao, A. Hazarika, L. T. Schelhas, J. Liu, E. A. Gaulding, G. Li, M. Zhang, M. F. Toney, P. C. Sercel and J. M. Luther, *ACS Energy Lett.*, 2020, **5**, 238–247.
25 Y. Bekenstein, B. A. Koscher, S. W. Eaton, P. Yang and A. P. Alivisatos, *J. Am. Chem. Soc.*, 2015, **137**, 16008–16011.
26 C. Chen, L. Zhang, T. Shi, G. Liao and Z. Tang, *Nanomaterials*, 2019, **9**, 21–27.
27 Z. Dang, J. Shamsi, F. Palazon, M. Imran, Q. A. Akkerman, S. Park, G. Bertoni, M. Prato, R. Brescia and L. Manna, *ACS Nano*, 2017, **11**, 2124–2132.
28 E. Hassanabadi, M. Latifi, A. F. Gualdrón-Reyes, S. Masi, S. J. Yoon, M. Poyatos, B. Julián-López and I. Mora-Seró, *Nanoscale*, 2020, **12**, 14194–14203.
29 L. Zhang, C. Kang, G. Zhang, Z. Pan, Z. Huang, S. Xu, H. Rao, H. Liu, S. Wu, X. Wu, X. Li, Z. Zhu, X. Zhong and A. K. Y. Jen, *Adv. Funct. Mater.*, 2021, **31**, 1–10.
30 C. C. Lin, S. K. Huang, C. E. Hsu, Y. C. Huang, C. Y. Wei, C. Y. Wen, S. S. Li, C. W. Chen and C. C. Chen, *J. Phys. Chem. Lett.*, 2020, **11**, 3287–3293.
31 J. Pan, Y. Shang, J. Yin, M. De Bastiani, W. Peng, I. Dursun, L. Sinatra, A. M. El-Zohry, M. N. Hedhili, A.-H. Emwas, O. F. Mohammed, Z. Ning and O. M. Bakr, *J. Am. Chem. Soc.*, 2018, **140**, 562–565.
32 C. de Weerd, L. Gomez, A. Capretti, D. M. Lebrun, E. Matsubara, J. Lin, M. Ashida, F. C. M. Spoor, L. D. A. Siebbeles, A. J. Houtepen, K. Suenaga, Y. Fujiwara and T. Gregorkiewicz, *Nat. Commun.*, 2018, **9**, 1–9.
33 T. Kirchartz, T. Markvart, U. Rau and D. A. Egger, *J. Phys. Chem. Lett.*, 2018, **9**, 939–946.
34 Z. Chen, L. Dong, H. Tang, Y. Yu, L. Ye and J. Zang, *CrystEngComm*, 2019, **21**, 1389–1396.
35 M. Liu, A. Matuhina, H. Zhang and P. Vivo, *Materials*, 2019, **12**, 3733.

36 A. Swarnkar, W. J. Mir and A. Nag, *ACS Energy Lett.*, 2018, **3**, 286–289.
37 J. Y. Woo, Y. Kim, J. Bae, T. G. Kim, J. W. Kim, D. C. Lee and S. Jeong, *Chem. Mater.*, 2017, **29**, 7088–7092.
38 B. Luo, Y.-C. Pu, S. A. Lindley, Y. Yang, L. Lu, Y. Li, X. Li and J. Z. Zhang, *Angew. Chem., Int. Ed.*, 2016, **55**, 8864–8868.
39 M. Pham and A. Travesset, *J. Chem. Phys.*, 2020, **153**, 204701.